Journal of Solid State Chemistry 184 (2011) 830–842

Contents lists available at ScienceDirect

Journal of Solid State Chemistry

journal homepage: www.elsevier.com/locate/jssc

Structure and magnetic order in the series $Bi_xRE_{1-x}Fe_{0.5}Mn_{0.5}O_3$ (RE=La,Nd)

C.A. Bridges [a,*], A.S. Sefat [b], E.A. Payzant [b], L. Cranswick [c,1], M.P. Paranthaman [a]

[a] Chemical Sciences Division, Oak Ridge National Laboratory, Oak Ridge, Building 4500 South, MS-6100, 1 Bethel Valley Road Oak Ridge, TN 37831-6100, USA
[b] Materials Science and Technology Division, Oak Ridge National Laboratory, Oak Ridge, TN 37831, USA
[c] Canadian Neutron Beam Centre, National Research Council of Canada, Chalk River Laboratories, Chalk River, Ontario, Canada K0J 1J0

ARTICLE INFO

Article history:
Received 30 December 2010
Accepted 7 February 2011
Available online 12 February 2011

Keywords:
Powder neutron diffraction
Crystal structure
Multiferroic
Perovskite
$Bi_xRE_{1-x}Fe_{0.5}Mn_{0.5}O_{3+\delta}$ (RE=La,Nd)
Antiferromagnetic
Bond valence

ABSTRACT

The influence of Bi^{3+} on the structural and magnetic properties of the rare-earth-containing perovskites $REFe_{0.5}Mn_{0.5}O_3$ (RE=La,Nd) was studied, and the limit of bismuth substitution was determined to be $x \leq 0.5$ in $Bi_xRE_{1-x}Fe_{0.5}Mn_{0.5}O_{3+\delta}$ (RE=La,Nd) at ambient pressure. Crystal structures in both La and Nd series were determined to be $GdFeO_3$-type *Pnma* with the exception of the $Bi_{0.3}La_{0.7}Fe_{0.5}Mn_{0.5}O_3$ sample, which is monoclinic *I2/a* in the $a^-b^-b^-$ tilt scheme. The samples undergo a transition to G-type antiferromagnetic order along with a weak ferromagnetic component, mixed with cluster-glass type behavior. The substitution of bismuth into the lattice results in a drop in T_N relative to the lanthanide end-members. Long range ordering temperatures T_N in the range 240–255 K were observed, with a significantly lower ordered magnetic moment in the case of lanthanum ($M \sim 1.7$–$1.9\ \mu_B$) than in the case of neodymium ($M \sim 2.1\ \mu_B$).

Published by Elsevier Inc.

1. Introduction

Due to both applied and fundamental interests, multiferroic materials in which ferroelectricity and ordered magnetism coexist have been intensely studied in recent years. This has involved the investigation of bulk materials such as $REMnO_3$ (RE=rare earth) perovskites, [1–3] wolframite-type $MnWO_4$, [4,5] spinel-type $(Co,Ni)Cr_2O_4$ and the hexagonal ferrite $Ba_2Mg_2Fe_{12}O_{22}$, [6] as well as the parallel investigation of magnetoelectric effects in multi-layered thin films [7–9]. The most intensely studied material has been $BiFeO_3$, as it combines a large spontaneous ferroelectric polarization with antiferromagnetic ordering above the room temperature, and it can be prepared at an ambient pressure [10–14]. Just as the stereochemically active lone-pair of the Bi^{3+} cation plays a critical role in the multiferroic properties displayed by $BiFeO_3$, many studies have examined the potential of cations containing a lone-pair to induce non-centrosymmetric symmetry (A-site-driven ferroelectrics) [15–18]. Despite the level of interest in this approach to design multiferroic phases, surprisingly few ambient-pressure perovskites (ABO_3) have been synthesized in bulk, in which the A-site contains pure Bi; these include $BiFeO_3$, $Bi_2Mn_{4/3}Ni_{2/3}O_6$, and $BiTi_{3/8}Fe_{1/4}M_{3/8}O_3$ (M=Mg,Ni) [19]. However, many more phases can be stabilized under high pressure, including $BiMO_3$ (M=Cr, Mn, Co, Ni, Al, In, Ga, Sc) and mixed B-site compositions such as $Bi(Mn_{1/2}Ni_{1/2})O_3$, $Bi(Mg_{1/2}Ti_{1/2})O_3$ and $Bi(Zn_{1/2}Ti_{1/2})O_3$ [20]. In addition to the search for new phases, understanding the effects of doping into known multiferroic phases in an attempt to enhance the desired properties has been a topic of keen interest [21–23].

Substitution of iron by manganese in the series $Bi(Fe_{1-x}Mn_x)O_3$ at an ambient pressure has been achieved up to $x \leq 0.3$, and has been shown to increase the magnetization and improve the dielectric properties of $BiFeO_3$ [24–25]. The series $Bi(Fe_{1-x}Mn_x)O_3$ for $0 \leq x \leq 1$ has been prepared under high pressure, and a phase diagram proposed; an unusual phase with lattice parameters $\sqrt{2}a_p \times 4a_p \times \sqrt{2}a_p$ was observed (a_p is the $\sim$4 Å parameter of the cubic perovskite subcell) in the composition range $0.2 \leq x \leq 0.6$, though the structure of this phase has not yet been determined [26]. The system $(BiFeO_3)_{1-x}(LaMnO_3)_x$ has been recently investigated by Lahmar et al., and it has been suggested that doping $LaMnO_3$ into thin films of $BiFeO_3$ may substantially improve the polarization and magnetic properties with respect to those of the parent phase $BiFeO_3$ [27,28]. The series $(BiFeO_3)_{1-x}(LaMnO_3)_x$ has been prepared in bulk by Gauglin et al. [29], where the $Bi_{0.5}La_{0.5}Fe_{0.5}Mn_{0.5}O_3$ member was reported to have a cubic symmetry, and more recently by Kundu et al. as a multiferroic *Pnma* ceramic [30]. While the centrosymmetric *Pnma* is not expected to support an electric polarization, there are other recent examples of compounds in which subtle distortions are reported to produce ferroelectric behavior in combination with a weak ferromagnetic moment [31,32]. In the case of *Pnma* $GdFeO_3$, ferroelectric behavior is reported to occur when exchange striction results in a cooperative displacement of the Gd^{3+} cation [31]. The perovskite

* Corresponding author. Fax: +1 865 574 4961.
E-mail address: bridgesca@ornl.gov (C.A. Bridges).
[1] Deceased.

0022-4596/$ - see front matter Published by Elsevier Inc.
doi:10.1016/j.jssc.2011.02.006

$YCrO_3$ exhibits a local distortion of the Cr^{3+} cation off the center of symmetry, resulting in weak ferroelectric-like polarization combined with a weak ferromagnetic moment below 140 K due to the canting of antiferromagnetic spins, despite the fact that the average structure appears to be centrosymmetric *Pnma* [32]. These examples demonstrate that subtle structural distortions may play an important role in the discovery of systems exhibiting a coupling of ferromagnetic and ferroelectric orders. Here, we determine the limit of Bi^{3+} substitution at an ambient pressure, and present a detailed study of its influence on the structure and magnetic properties of the rare-earth-containing perovskites $REFe_{0.5}Mn_{0.5}O_3$ (*RE*=La,Nd).

2. Experimental

2.1. Synthesis

A stoichiometric mixture of Bi_2O_3 (Aldrich, 99.999%), Fe_2O_3 (Aldrich, 99.999%), Mn_2O_3 (Aldrich, 99.999%), and La_2O_3 (Alfa Aesar, 99.99%) or Nd_2O_3 (Alfa Aesar, 99.99%) was intimately ground, pelletized and fired at increasing temperatures. Initial firing was performed at 1073 K on all samples, with final firing temperatures of 1173 K for $Bi_{0.5}Nd_{0.5}Fe_{0.5}Mn_{0.5}O_3$, 1223 K for $Bi_{0.3}RE_{0.7}Fe_{0.5}Mn_{0.5}O_3$ and $Bi_{0.5}La_{0.5}Fe_{0.5}Mn_{0.5}O_3$, and 1323 K for $Bi_{0.1}La_{0.9}Fe_{0.5}Mn_{0.5}O_3$. It was necessary to lower the maximum firing temperature for $Bi_{0.1}Nd_{0.9}Fe_{0.5}Mn_{0.5}O_3$ to obtain a pure phase. The reagents in the synthesis of $Bi_{0.1}Nd_{0.9}Fe_{0.5}Mn_{0.5}O_3$ were dissolved in dilute nitric and hydrochloric acids to improve cation mixing, dried at 383 K, reground, and then fired at 673 K for 24 h; this was followed by pelletizing and firing at 1073 K for 24 h, and by regrinding and firing at 1173 K for 12 h to obtain a pure phase. All samples were quenched by removing them directly from the furnace at their final firing temperature. Impurity levels increased significantly for Bi doping levels above $x=0.5$ for both the neodymium- and the lanthanum-containing series, and therefore were not further investigated.

2.2. Powder X-ray diffraction

Powder X-ray diffraction (XRD) data were obtained using a Panalytical X-pert Pro diffractometer with Cu $K\alpha$ radiation. Powder samples were dispersed on a flat plate and data were collected in Bragg-Brentano geometry.

2.3. Powder neutron diffraction

Powder neutron diffraction (PND) data were collected on the C2 diffractometer operated by the National Research Council of Canada at the Chalk River Laboratories of Atomic Energy of Canada Limited (AECL). The data collection strategy involved obtaining high angle (34.8–114.8° 2θ) data at a refined wavelength of 1.33091(5) Å, in conjunction with low angle (3.4–83.4° 2θ) data at a wavelength of 2.3726(1) Å at temperatures of 300 and 4 K. This strategy maximized the *d*-spacing range available for the analysis of both crystal and magnetic structures. Data were further collected in a closed-cycle refrigerator in 10 or 15 K increments below 50 K, 25 K increments to 150 K, 10 K increments up to ~220 K (~30 K below Néel temperature), 5 K increments around the magnetic ordering temperature, and further 10 K increments up to 300 K. Data above 4 K and below 300 K were collected in the low angle range at 2.3726 Å to follow the evolution of the ordered magnetic moment. Data for the sample $Bi_{0.1}Nd_{0.9}Fe_{0.5}Mn_{0.5}O_3$ were collected at 300 K on the POWGEN beamline at the Spallation Neutron Source (SNS).

X-ray and neutron powder diffraction data were analyzed for unit cell constants, phase fractions and structural information using Rietveld refinement [33] with GSAS/EXPGUI [34,35] and Fullprof/WinPLOTR [36,37]. Variable temperature data were analyzed using the cyclic refinement capabilities of Fullprof based upon a starting model obtained at 4 K.

2.4. DC magnetic susceptibility measurements

Magnetic susceptibility data were collected in 1 K increments from 2 to 50 K, and in 3 K increments from 50 to 350 K, using a Quantum Design MPMS SQUID magnetometer at applied magnetic fields of either 0.1 or 1 T. The powder sample was contained with a gelatin capsule.

2.5. Electron microprobe measurements

Electron microprobe data were collected using a JEOL 8200 5-spectrometer electron microprobe with JEOL EDS at the High Temperature Materials Laboratory (HTML) of Oak Ridge National Laboratory (ORNL).

3. Results and discussion

3.1. Electron microprobe

Electron microprobe results indicated that the samples were predominantly homogeneous on the micron scale, and that the average stoichiometries agreed within an error with the target cation compositions (Table 1 and Fig. S1). Annealing at higher temperature did not ensure homogeneity, but instead promoted decomposition at higher temperatures; in fact, a sample of $Bi_{0.1}Nd_{0.9}Fe_{0.5}Mn_{0.5}O_3$ annealed at 1323 K for 10 h with intermediate regrinding displayed phase segregation, leading to manganese- and iron-rich phases (Fig. S2). Therefore, the final firing temperatures selected for each sample to the temperature were those at which impurity peaks were minimized. Residual chlorine contamination at a level of approximately 0.01 mol per formula unit was observed in the $Bi_{0.1}Nd_{0.9}Fe_{0.5}Mn_{0.5}O_3$ sample derived from the dissolution of starting reagents. Impurities were observed at low levels (~1–2 wt%) in all samples; typically, β-Bi_2O_3 was the main impurity, though other phases such as mullite-type $Bi_2(Mn,Fe)_4O_9$ or sillenite-type $Bi_{12}(Mn,Fe)O_{20}$ may also occur. The dominant impurities were included in Rietveld refinements for samples reported here, and their refined weight percentages are included in Table 2.

3.2. Crystal structure

Combined Rietveld refinements for the series $Bi_xRE_{1-x}Fe_{0.5}Mn_{0.5}O_3$ ($x=0.1$, 0.3, 0.5) were performed using powder X-ray and neutron diffraction data collected at room temperature. The collected X-ray diffraction data are presented in Figs. 1 and S3,

Table 1
Electron microprobe results for $Bi_xRE_{1-x}Fe_{0.5}Mn_{0.5}O_3$ ($x=0.1$, 0.3, 0.5).

Nominal stoichiometry	Bi	*RE*	Fe	Mn[a]	O
$Bi_{0.5}La_{0.5}Fe_{0.5}Mn_{0.5}O_3$	0.51(2)	0.47(2)	0.52(2)	0.50(2)	2.86(13)
$Bi_{0.3}La_{0.7}Fe_{0.5}Mn_{0.5}O_3$	0.31(2)	0.68(3)	0.51(2)	0.50(2)	2.87(11)
$Bi_{0.1}La_{0.9}Fe_{0.5}Mn_{0.5}O_3$	0.087(4)	0.85(4)	0.51(2)	0.50(2)	2.74(12)
$Bi_{0.5}Nd_{0.5}Fe_{0.5}Mn_{0.5}O_3$	0.52(2)	0.53(2)	0.49(2)	0.50(2)	2.82(12)
$Bi_{0.3}Nd_{0.7}Fe_{0.5}Mn_{0.5}O_3$	0.31(1)	0.75(3)	0.49(2)	0.50(2)	2.96(12)
$Bi_{0.1}Nd_{0.9}Fe_{0.5}Mn_{0.5}O_3$	0.10(1)	0.85(3)	0.48(2)	0.50(2)	3.17(12)

[a] Values are normalized against Mn.

Table 2
Refinement results for $Bi_xRE_{1-x}Fe_{0.5}Mn_{0.5}O_3$ (x=0.1, 0.3, 0.5) with structural parameters obtained at 300 K.

		La			Nd		
Sample		x=0.1	0.3	0.5	x=0.1	0.3	0.5
Space group		*Pnma*	*I2/a*	*Pnma*	*Pnma*	*Pnma*	*Pnma*
Lattice parameters[a]	a (Å)	5.5185(1)	7.8201(1)	5.54366(5)	5.57584(5)	5.63523(3)	5.60647(6)
	b (Å)	7.8153(2)	5.56126(5)	7.82919(6)	7.72696(6)	7.73337(3)	7.77011(8)
	c (Å)	5.5501(1)	5.52923(7)	5.56372(4)	5.44263(4)	5.43789(2)	5.44564(6)
	β (°)	–	90.182(1)°	–	–	–	–
	V (Å^3)	239.370(6)	240.462(5)	241.479(3)	234.492(5)	236.979(2)	237.228(6)
Magnetic order	T_N (K) – PND[b]	243(2)	241(1)	243(2)	–	253(2)	252(1)
	T_N (K) – χ_m	245	239	246	240	254	242
	M (μ_B)	1.66(4)	1.88(2)	1.81(2)	–	2.14(3)	2.15(2)
	B	0.28(2)	0.32(1)	0.27(2)	–	0.26(2)	0.34(1)
Statistical fit	χ^2	2.317	2.118	2.124	3.659	2.834	2.258
	wRp	0.0888	0.0820	0.0722	0.0443	0.0884	0.0784
	Rp	0.0644	0.0582	0.0536	0.0294	0.0645	0.0566
Fractional coordinates	Bi/*RE x*	0.5161(1)	0.25	0.5115(1)	0.5473(1)	0.5529(1)	0.5488(1)
	Bi/*RE y*	0.25	0.9989(4)	0.25	0.25	0.25	0.25
	Bi/*RE z*	0.5028(3)	0.00	0.5045(2)	0.5089(1)	0.5091(1)	0.5071(2)
	O1 x	0.9947(7)	0.25	0.9969(10)	0.9819(1)	0.9785(4)	0.9791(4)
	O1 y	0.25	0.4381(7)	0.25	0.25	0.25	0.25
	O1 z	0.4352(6)	0.00	0.4309(5)	0.4191(2)	0.4145(5)	0.4170(5)
	O2 x	0.7310(4)	0.4650(3)	0.7321(6)	0.2969(1)	0.3010(3)	0.2987(2)
	O2 y	0.9646(3)	0.734(1)	0.9641(2)	0.0427(1)	0.0442(2)	0.0422(2)
	O2 z	0.2675(5)	0.264(1)	0.2669(6)	0.7091(1)	0.7071(3)	0.7043(3)
ADP	Bi/*RE*	0.0112(2)	0.0193(2)	0.0276(2)	0.0148(1)	0.0167(2)	0.0148(2)
	Mn/Fe	0.001	0.001	0.0032(2)	0.0096(2)	0.0098(3)	0.0031(3)
	O	0.0113(2)	0.0194(3)	0.0242(3)	0.0127(1)	0.0120(3)	0.0127(3)
Phase fractions	ABO_3	99.3(1)%	99.21(3)%	99.64(2)%	100%	99.2(2)%	99.2(2)%
	$Bi_2(Mn,Fe)_4O_9$	0.7(1)%	N/A	N/A	N/A	N/A	N/A
	β-Bi_2O_3	N/A	0.79(3)%	0.36(2)%	N/A	0.8(2)%	0.8(2)%

[a] All crystallography data are for the combined refinement of neutron and X-ray powder diffraction data at 300 K; M is the refined moment at 4 K; the ADP for the Mn/Fe site for Bi content of x=0.1 and 0.3 (*RE*=La) were fixed at small positive values as they tended to attain a small negative (unphysical) value; the phase fraction is given as a weight percent.

[b] T_N is the magnetic ordering temperature. It was estimated from powder neutron diffraction data (PND) by fitting to a critical exponent function, and from χ_m data based upon the minimum in a plot of $\delta(\chi T)/\delta T$.

fits to the powder neutron diffraction data for *RE*=La in Fig. 2 and for *RE*=Nd in Fig. 3. Rietveld refinement results are presented in Tables 2 and 3 for the lanthanum- and neodymium-containing samples. Based upon the electron microprobe results, the occupancies have been constrained to the nominal values. However, the effects of refining site occupancies have been investigated, and are described below. The structures determined at 4 K for $Bi_xRE_{1-x}Fe_{0.5}Mn_{0.5}O_3$ (x=0.1, 0.3, 0.5) are identical to those observed at 300 K. There is no evidence from the refined data to indicate a structural phase transition for any sample in the temperature range 4–300 K.

The phase β-Bi_2O_3 was the dominant impurity in the x=0.3 and 0.5 phases, present at a refined level of ~0.8% by weight or less; the $Bi_{0.1}La_{0.9}Fe_{0.5}Mn_{0.5}O_3$ sample contained a $Bi_2Fe_4O_9$-type impurity phase. One weak peak (~1–2% intensity) was typically present in samples at ~31.0° 2θ that corresponded closely to a peak expected from a $Bi_2Fe_4O_9$-type impurity phase, though this assignment was not conclusive due to the low contribution of this peak to the patterns, which resulted in the peak intensity being poorly fitted by Rietveld refinements; a weak peak at ~1% intensity relative to the main reflection was also present in all the X-ray diffraction data, due to an incomplete filtering of Cu $K\beta$ radiation. Increases in the levels of bismuth-containing impurity phases were observed beyond x=0.5 in both lanthanum- and neodymium-containing series, in addition to the presence of a rhombohedral phase in some samples. Due to the presence of significant impurities, these samples were not pursued further.

The phases $x \leq 0.5$ for *RE*=La and Nd could be well described in the $GdFeO_3$-type structure with space group *Pnma* (tilt system $a^+b^-b^-$ in Glazer notation [38–42]), with the exception of the $Bi_{0.3}La_{0.7}Fe_{0.5}Mn_{0.5}O_3$ sample (discussed below). These bismuth doped phases therefore have structures related to the parent compounds $LaFe_{0.5}Mn_{0.5}O_3$ and $NdFe_{0.5}Mn_{0.5}O_3$, which are also reported to be *Pnma* [43–44]. It is interesting to note that the composition $LaFe_{0.5}Mn_{0.5}O_3$ is positioned in the $La(Mn_xFe_{1-x})O_3$ series near to a phase boundary between orthorhombic *Pnma* and rhombohedral $R\bar{3}c$, which occurs for $0.6 < x < 1.0$ [45], while the ambient pressure phases $Bi(Fe_{1-x}Mn_x)O_3$ for $x \leq 0.3$ exhibit the $BiFeO_3$ rhombohedral $R\bar{3}c$. As a result, the $Bi_xLa_{1-x}Fe_{0.5}Mn_{0.5}O_3$ series sits close in composition to a higher symmetry rhombohedral structure, which likely led to the original assignment of the $Bi_{0.5}La_{0.5}Fe_{0.5}Mn_{0.5}O_3$ phase as cubic [29]. However, results of this study indicate that it is not possible under ambient pressure conditions to substitute sufficient bismuth to promote the formation of a rhombohedral phase, or the formation of a phase similar to the high-pressure orthorhombic $Bi(Fe_{0.5}Mn_{0.5})O_3$ structure [26], from either lanthanide end-member.

The *B*-site position typically exhibited negative atomic displacement parameters (ADP) in the refinements of the XRD data, as compared to the positive values typically observed in refinements of the neutron diffraction data. This is a common issue when refining the XRD data of highly absorbing samples collected in Bragg-Brentano geometry. Therefore, in combined refinements of the XRD and neutron diffraction data, an absorption correction for surface roughness in Bragg-Brentano geometry was applied to the X-ray diffraction data for each sample [46]. This correction increased the magnitude of the ADPs in the combined refinement in such a way that they approached the values found in an

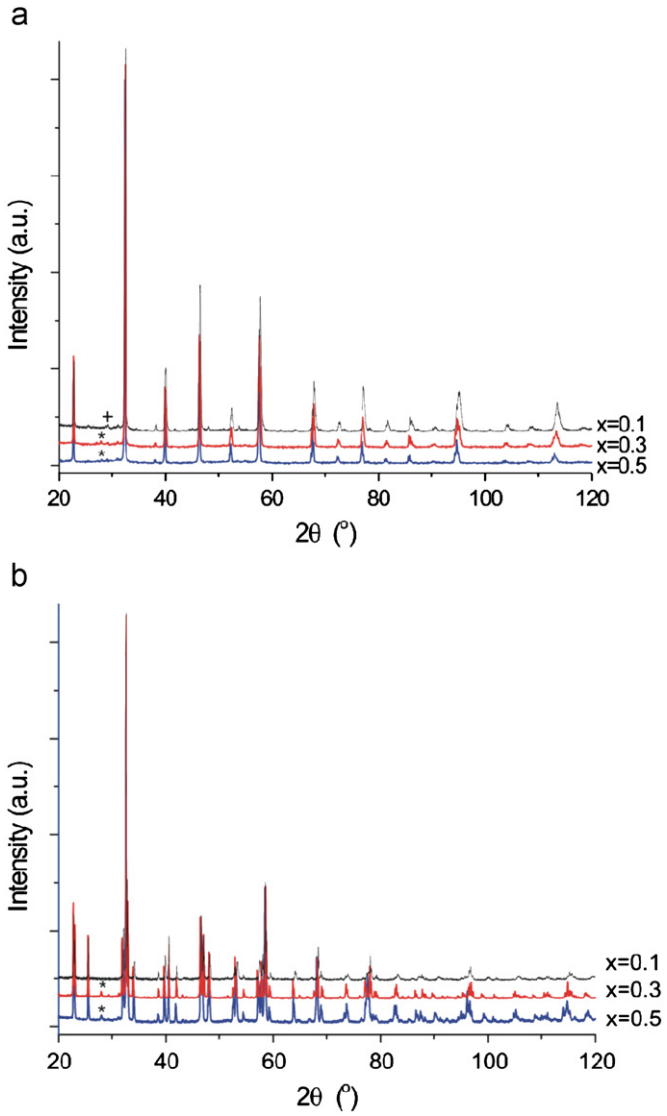

Fig. 1. Powder X-ray diffraction data for $Bi_xRE_{1-x}Fe_{0.5}Mn_{0.5}O_3$, where (a) *RE*=La, and (b) *RE*=Nd. The plus symbol indicates a $Bi_2Fe_4O_9$-type impurity (for *RE*=La), while the stars indicate β-Bi_2O_3 impurity.

independent refinement of the neutron data. In some cases, in particular for $Bi_{0.5}La_{0.5}Fe_{0.5}Mn_{0.5}O_3$, the ADPs of the *A*- and *O*-sites were slightly higher than expected. The larger ADP can be indicative of difficulties with the model (e.g., incorrect symmetry), problems with the data correction (e.g. absorption correction), static disorder, or dynamic disorder. Refinement of the 4 K data showed a similarly large ADP, indicating that this was not an effect of dynamic disorder. In the case of $Bi_{0.5}La_{0.5}Fe_{0.5}Mn_{0.5}O_3$ ($ADP_{A\text{-site}} \sim 0.028$ Å^2), the effects of lowering the space group symmetry to monoclinic $P2_1/n$ and $I2/a$ were investigated, and did not improve the fit or reduce the size of the ADP on the *A*-site. It is possible that the lone-pair of electrons present for Bi^{3+} could exert pressure on the local symmetry, resulting in a local distortion in which bismuth moves off the higher symmetry *A*-site position [47]. Attempts to model a distortion of this type with a separate Bi^{3+} site did not improve the fit significantly or reduce the size of the ADP, and it was not clear from the available data that a larger cell due to a cooperative distortion was present; a long range cooperative distortion would likely be quenched by the presence of La^{3+} on the *A*-site. The large ADP may therefore relate to difficulties in fitting the absorption properly, or to a static random disorder on the *A*-site related to the lone-pair of Bi^{3+}.

Broad peaks are observed in the background in the XRD data and the PND data of all samples near to the (0 1 1) and (2 0 2) reflection positions at less than 1% of the maximum peak intensity (Fig. S4); e.g., this corresponds to 2θ positions near 30° and 63°, respectively, for the 2.37 Å data in Figs. 2 and 3. The reflections have a full width at half maximum (FWHM) of roughly 5°, as compared to 0.7° at low angle for the main phase in the XRD data. While these broad peaks are near positions, where magnetic reflections occur below the magnetic ordering temperature, this broadening is observed at all temperatures, indicating a non-magnetic origin; short range magnetic order would be expected to vary at temperatures far above or below T_N. Therefore, this may indicate an intermediate range order, resulting from domains of oxygen order or cation order, or to poor crystallinity in a fraction of the sample.

Variation from the nominal stoichiometry has been investigated using combined Rietveld refinements of the XRD and PND data. In the refinements reported in Table 4, the transition metal (*B*-site) and the lanthanide (*A* site) occupancies were held constant, and the bismuth and oxygen site occupancies were refined, producing an improvement in the fit. The ADP values and goodness-of-fit indicator χ^2 are included for comparison with the refinements of fixed nominal stoichiometry. The ADP values were modified only slightly from the refinement in fixed stoichiometry, and no significant reduction in the large ADP of samples such as $Bi_{0.5}La_{0.5}Fe_{0.5}Mn_{0.5}O_3$ was observed. A deficiency of Bi^{3+} is generally observed in the lanthanum-containing samples. Such a deficiency may be expected, as the main impurities were observed to be bismuth-containing phases in both the diffraction data and the microprobe analysis, and as a low level of bismuth evaporation may occur in the higher temperature firings. For the neodymium series of samples, the refined occupancy of bismuth was above the nominal content; this surprising result suggests that there is a deficiency on the *B*-site relative to the *A* site. No evidence has been found in the data for the presence of significant transition metal-oxide impurities, suggesting that the apparent Bi^{3+} excess may be an artifact of the refinement. The results of combined refinement of oxygen and bismuth site occupancies suggest an excess of oxygen relative to the nominal composition, which must lead to an oxidized *B*-site in order to maintain charge neutrality (i.e. the formation of Mn^{4+}); oxygen excess is defined relative to the expected oxygen content for a sample, in which only Mn^{3+} is present. For all compounds $Bi_xRE_{1-x}Fe_{0.5}Mn_{0.5}O_{3+\delta}$ oxygen excess (δ) in the range 0.001–0.405 was refined. Oxygen excess was also observed in refinements of the neutron diffraction data alone, which are more sensitive to the oxygen content than the XRD data. Such oxygen excess has been observed in manganate perovskites, including $BiMnO_{3+\delta}$, $LaMnO_{3+\delta}$, and $Bi(Fe_{1-x}Mn_x)O_3$ (for $x \leq 0.3$), and is interpreted as indicating a cation deficiency in the perovskite lattice due to the lack of available sites for excess oxygen in the idealized structure [24]. The level of oxygen excess observed by Rietveld refinement of some samples reported here (up to $\delta \sim 0.405$ according to PND) is rather high for a sample heated in air and quenched to room temperature, as compared with similar results for $LaMnO_{3+\delta}$, in which an oxygen excess of $\delta=0.05$ is found when fired in air at 1273 K, and $\delta=0.18$ when fired in an O_2 at 1073 K [48]. As shown in Table 4, the higher levels of oxygen excess suggest that all of the manganese is in the 4+ state; in some cases, the level of oxygen excess is not possible as it would require greater amount of manganese than available in order to achieve charge balance. This suggests that an attempt to provide a fully quantitative analysis of the site occupancy from Rietveld refinement for these samples must be taken with care. However, it is interesting to note that the nominal $Bi_{0.1}Nd_{0.9}Fe_{0.5}Mn_{0.5}O_3$ sample exhibits an oxygen excess of only $\delta=0.001$, and refined occupancies are very close to the nominal values.

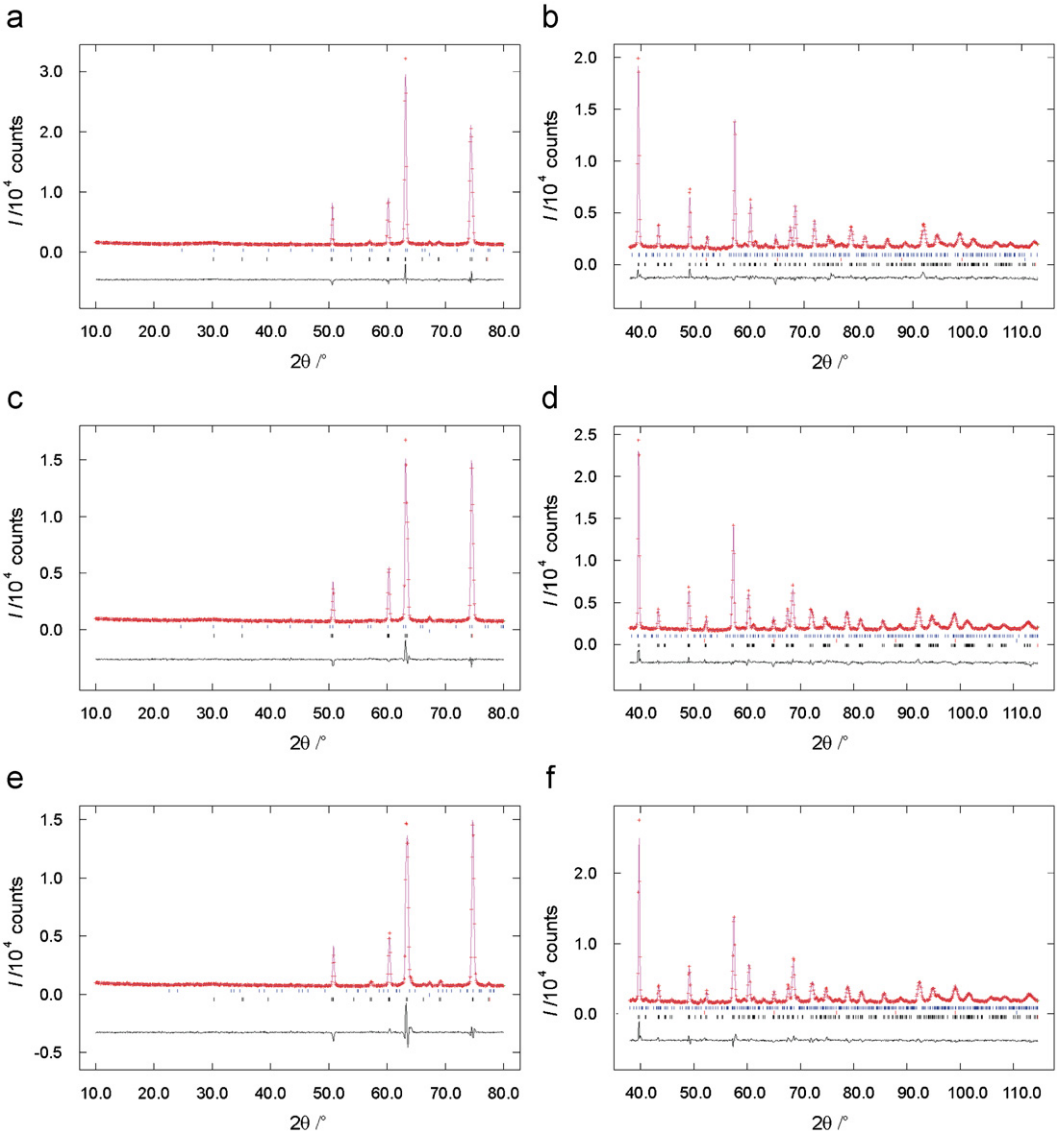

Fig. 2. Rietveld refinement of powder neutron diffraction data collected at 300 K for $Bi_xLa_{1-x}Fe_{0.5}Mn_{0.5}O_3$ at a wavelength of 2.37 Å (left) and 1.33 Å (right), for $x=0.5$ (a/b), 0.3 (c/d), and 0.1 (e/f). Reflection markers are given below the patterns for the perovskite phase (bottom), the vanadium sample can (middle), and minor impurity phase (top; $Bi_2(Mn,Fe)_4O_9$ or β-Bi_2O_3).

This may be related to the particular conditions of the sample preparation given that the firing protocol is quite sample specific, or to the fact that only these data were collected at the higher resolution beamline.

3.3. Bond valence sums

Bond valence calculations were undertaken to examine the oxidation state of manganese and iron, as well as the coordination environments of the *A* and *O* sites, on the basis of crystallographic bond lengths. There has been a discussion in the literature recently concerning the appropriate bond valence parameters for cations containing a lone-pair of electrons, such as the Bi^{3+} 6*s* lone-pair [49–51]. The equation used to calculate bond valence is

$$S = \exp((R_o - R)/b) \quad (1)$$

where *S* is the experimental bond valence, *R* is the observed bond length, and R_o and *b* are bond valence parameters specific to each cation oxidation state and chemical environment. It has been suggested that when calculating the bond valence sum around Bi^{3+} that a value for *b* of 0.5 may be more appropriate than 0.37, which is currently used as a universal constant for all cations and cation environments. The choice of *b* parameter for Bi^{3+} influences the bond valence sums for the *A*, *O*1 and *O*2 sites, but not for the *B*-site. Therefore, the impact of *b* value is shown in Tables 5 and 6 for the lanthanum and neodymium series, respectively, and the *B*-site results for all samples are given in Table 7. The use of $b=0.5$ appears to bring the average bond valence sums (BVS) for the *A*- and *O*-sites significantly closer to the nominal values of 3+ and 2−. The remaining differences may reflect the difficulty in finding universal values of *b* and R_o for Bi^{3+} that will reflect the differing stereochemical influence of the lone-pair in different environments; the greater level of octahedral tilting in the neodymium samples versus the lanthanum-containing samples may provide greater opportunity for relief of the octahedral strain induced by the lone-pair, resulting in a BVS closer to 3+. The average BVSs for the *A*-site of $Bi_xLa_{1-x}Fe_{0.5}Mn_{0.5}O_3$ samples may be brought in the range 2.89+ to 3.09+ by including the longer (> 3 Å) bonds between the *A*-site (Bi and La) and oxygen (see Table S1), with lengths on the order of metal–metal distances ($d_{A\text{-site-to-}B\text{-site}} \sim 3.2$–$3.4$ Å). For very long bonds, these may be considered as *tertiary* bonds to the secondary coordination sphere of oxygen [49]. The longer ~3.1–~3.2 Å A–O bonds are near the

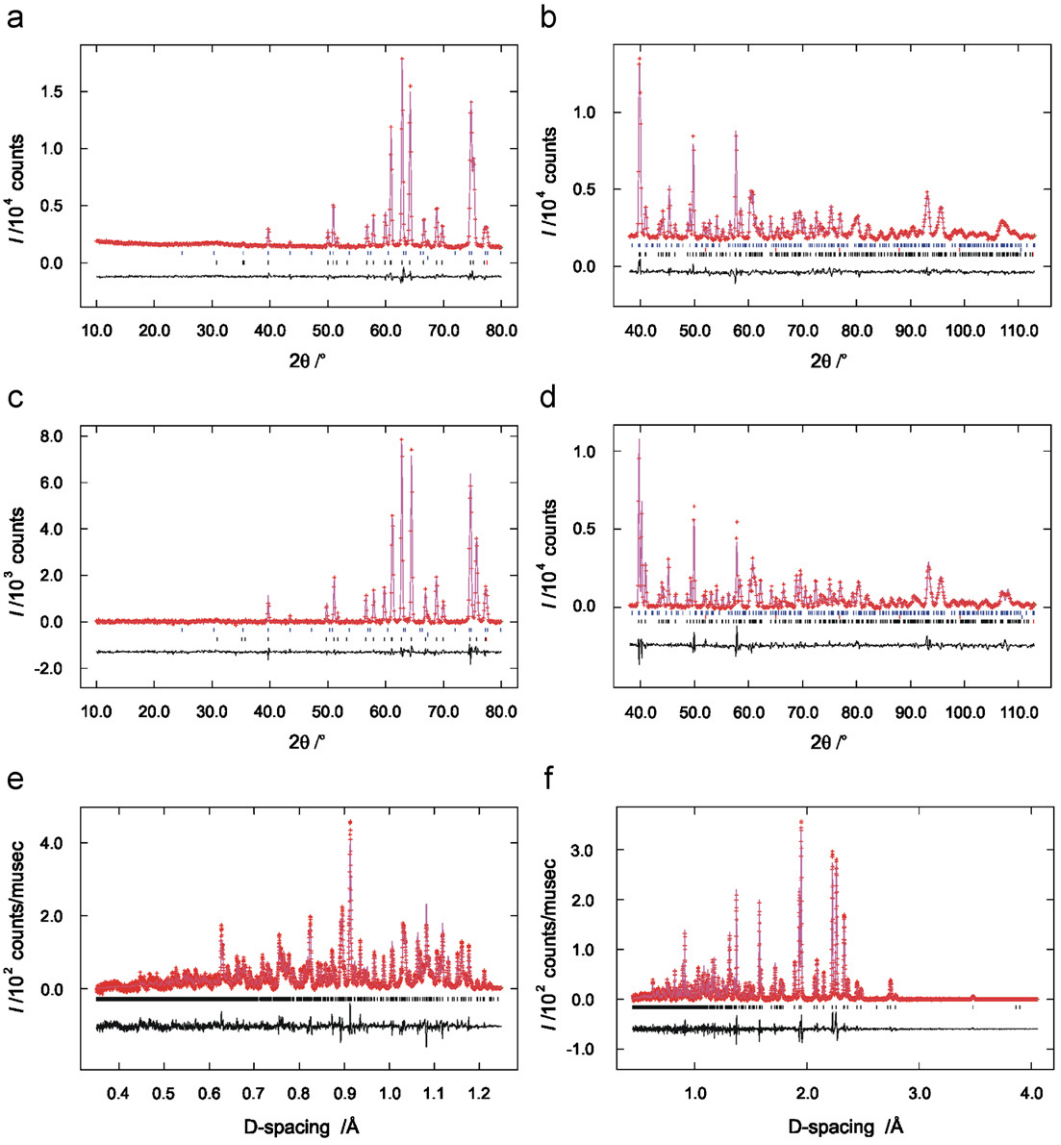

Fig. 3. Rietveld refinement of powder neutron diffraction data collected at 300 K for $Bi_xNd_{1-x}Fe_{0.5}Mn_{0.5}O_3$ at a wavelength of 2.37 Å (left) and 1.33 Å (right), for $x=0.5$ (a/b), and $x=0.3$ (c/d). Reflection markers are given below the patterns for the perovskite phase (bottom), the vanadium sample can (middle), and minor β-Bi_2O_3 impurity phase (top). Data in (e) and (f) are diffraction data for $x=0.1$ collected at 300 K on the POWGEN beamline at the SNS.

Table 3
Bond distances and bond angles for $Bi_xRE_{1-x}Fe_{0.5}Mn_{0.5}O_3$ at 300 K.

RE	La			Nd		
x	0.1	0.3	0.5	0.1	0.3	0.5
Angles						
M–O_1–*M*	159.1(1)	160.1(2)	157.8(2)	153.7(1)	152.1(2)	153.0(1)
M–O_2–*M*	161.8(1)	162.7(1)	161.9(1)	152.6(1)	151.3(1)	151.6(1)
Distances						
M-O_1(×2)	1.9866(1)	1.9848(7)	1.9948(6)	1.9839(2)	1.9921(7)	1.9978(6)
M–O_2(×2)	1.986(1)	1.975(7)	1.992(4)	2.036(1)	2.064(2)	2.037(1)
M–O_2(×2)	1.977(1)	1.991(7)	1.985(4)	1.974(1)	1.978(2)	1.994(1)
	1.983	1.984	1.991	1.998	2.011	2.010

edge of the primary coordination sphere, and may prove necessary in general to obtain a proper average BVS for these materials.

The calculated bond valence sums in Table 7 are consistent with *B*-sites containing a mixture of Fe^{3+}, Mn^{3+}, and Mn^{4+} for all samples. The presence of Mn^{4+} is indicated by an average BVS greater than 3+ on the *B*-site, and is significantly higher for the lanthanum-containing samples (3.21+ to 3.28+) than for the neodymium samples (3.05+ to 3.16+). The levels of oxygen excess suggested by these results are much closer to what might be expected for a manganate perovskite than what was derived earlier from Rietveld refinements of the occupancies. The results confirm that a significant level of oxidation of Mn^{3+}–Mn^{4+} is present, corresponding to an oxygen excess of $\delta\sim0.05$–0.07 for lanthanum samples and $\delta\sim0.01$–0.04 for the neodymium samples.

3.4. Crystal structure of $Bi_{0.3}La_{0.7}Fe_{0.5}Mn_{0.5}O_3$

A sample of this composition was refined in the $GdFeO_3$-type structure of the other phases, and was observed to fit poorly (Fig. 4). Subsequent LeBail fitting in related rhombohedral and monoclinic cells demonstrated a superior fit could be obtained with a monoclinic distortion. The improvement in a monoclinic cell was particularly apparent in the higher resolution of the X-ray diffraction data. The space group $P2_1/n$, a subgroup of *Pnma*, was examined to investigate whether the monoclinic distortion

Table 4
Summary of fractional occupancies derived from Rietveld refinement for $Bi_xRE_{1-x}Fe_{0.5}Mn_{0.5}O_{3+\delta}$ samples.

Composition	δ	ADP (× 100 Å^2)			χ^2
		Bi	Mn/Fe	O	
$Bi^{3+}_{0.490}La^{3+}_{0.5}Mn^{3+}_{0.000}Mn^{4+}_{0.500}Fe^{3+}_{0.5}O_{3.251}$	0.267	2.60(2)	0.28(4)	3.03(4)	2.060
$Bi^{3+}_{0.251}La^{3+}_{0.7}Mn^{3+}_{0.000}Mn^{4+}_{0.500}Fe^{3+}_{0.5}O_{3.206}$	0.279	1.60(2)	0.10	2.40(4)	2.021
$Bi^{3+}_{0.060}La^{3+}_{0.9}Mn^{3+}_{0.000}Mn^{4+}_{0.500}Fe^{3+}_{0.5}O_{3.345}$	0.405	0.84(2)	0.09(3)	1.74(3)	2.151
$Bi^{3+}_{0.523}Nd^{3+}_{0.5}Mn^{3+}_{0.291}Mn^{4+}_{0.209}Fe^{3+}_{0.5}O_{3.139}$	0.105	1.45(2)	0.10	1.41(4)	2.243
$Bi^{3+}_{0.369}Nd^{3+}_{0.7}Mn^{3+}_{0.000}Mn^{4+}_{0.500}Fe^{3+}_{0.5}O_{3.450}$	0.347	1.43(2)	0.06(5)	1.58(4)	2.719
$Bi^{3+}_{0.108}Nd^{3+}_{0.9}Mn^{3+}_{0.497}Mn^{4+}_{0.003}Fe^{3+}_{0.5}O_{3.014}$	0.001	1.50(1)	0.91(2)	1.27(1)	3.657

Table 5
A- and *O*-sites bond valence results for $Bi_xLa_{1-x}Fe_{0.5}Mn_{0.5}O_3$ at 300 K.

$b_{A\text{-site}}$	0.37			0.5		
x	0.1	0.3	0.5	0.1	0.3	0.5
BVS_{Bi}	2.108	2.030	2.082	3.025	2.936	2.990
BVS_{RE}	2.602	2.507	2.570	2.602	2.507	2.570
$BVS_{Ave\ A}$	**2.553**	**2.364**	**2.326**	**2.645**	**2.635**	**2.780**
BVS_{O1}	1.957	1.897	1.854	1.987	1.987	2.003
BVS_{O2}	1.937	1.871	1.842	1.968	1.961	1.995
$BVS_{Ave\ O}$	**1.947**	**1.884**	**1.848**	**1.977**	**1.974**	**1.999**

*Note that weighted averages of the bond valence sum are reported for the *A* site.

Table 6
A- and *O*-sites bond valence results for $Bi_xNd_{1-x}Fe_{0.5}Mn_{0.5}O_3$ at 300 K.

$b_{A\text{-site}}$	0.37			0.5		
x	0.1	0.3	0.5	0.1	0.3	0.5
BVS_{Bi}	2.630	2.673	2.618	3.469	3.510	3.454
BVS_{RE}	2.799	2.844	2.786	2.799	2.844	2.786
$BVS_{Ave\ A}$	**2.782**	**2.758**	**2.702**	**2.866**	**3.177**	**3.120**
BVS_{O1}	1.990	1.987	2.959	2.011	2.090	2.063
BVS_{O2}	1.974	1.912	1.900	2.006	2.070	2.057
$BVS_{Ave\ O}$	**1.982**	**1.950**	**1.930**	**2.008**	**2.080**	**2.060**

*Note that weighted averages of the bond valence sum are reported for the *A* site.

Table 7
B-site bond valence results for $Bi_xRE_{1-x}Fe_{0.5}Mn_{0.5}O_3$ at 300 K.

RE	La			Nd		
x	0.1	0.3	0.5	0.1	0.3	0.5
$BVS_{Mn(III)}$	3.283	3.279	3.217	3.161	3.057	3.061
$BVS_{Fe(III)}$	3.274	3.270	3.209	3.153	3.049	3.053
$BVS_{Ave\ M1}$	**3.278**	**3.275**	**3.213**	**3.157**	**3.053**	**3.057**
$BVS_{Mn(IV)}$	3.221	3.218	3.157	3.102	3.000	3.004
$BVS_{Fe(II)}$	3.060	3.057	2.999	2.947	2.849	2.853
$BVS_{Ave\ M2}$	**3.141**	**3.137**	**3.078**	**3.024**	**2.925**	**2.929**

could relate to rock-salt ordering on the B sublattice, combined with tilting of BO_6 (*B*=Fe,Mn) octahedra. While a good fit was obtained in $P2_1/n$ (χ^2=2.155, *wRp*=0.0827), little ordering of Fe and Mn was observed in the refinement, and additional constraints on the *A* site position were required to obtain convergence (the *x* parameter was fixed at a high symmetry position). Given the need to constrain the *A* site position, the higher symmetry centrosymmetric monoclinic supergroups *C*2/*m* and *C*2/*c* were examined. Similarly it proved difficult to obtain convergence in space group *C*2/*m* without constraining the *A* site position. However, *I*2/*a* (standard setting *C*2/*c*) resulted in improved goodness-of-fit indicators (χ^2=2.118, *wRp*=0.0820) relative to $P2_1/n$, and requiring no additional constraints on the *A* site position (Fig. 4). Given the equivalent systematic absences of *Cc*, a refinement was performed in this noncentrosymmetric space group; in this case, it was impossible to obtain convergence without constraining the *A* site position. An examination of the *I*2/*a* structure with the ADDSYM function in the program PLATON [52,53] did not reveal any additional symmetry. Rietveld refinement results indicate that the centrosymmetric space group *I*2/*a* is the correct space group for $Bi_{0.3}La_{0.7}Fe_{0.5}Mn_{0.5}O_3$.

Additional consideration was given to the possibility that the sample could be composed of a mixture of *Pnma* and *I*2/*a* phases. There are few peaks in either the neutron diffraction or X-ray diffraction data to clearly indicate the change in symmetry due to the significant peak overlap, and had given rather subtle differences in atomic positions between the two space groups, the best evidence for the *I*2/*a* space group comes from the much improved Rietveld fit. For example, the (2 0 1)/(1 0 2) peaks present near 57° 2θ (*d*-spacing ≈ 2.48 Å in Fig. 2) in the long wavelength neutron diffraction data for $Bi_{0.1}La_{0.9}Fe_{0.5}Mn_{0.5}O_3$ and $Bi_{0.5}La_{0.5}Fe_{0.5}Mn_{0.5}O_3$ are not clearly present in the neutron diffraction data for $Bi_{0.3}La_{0.7}Fe_{0.5}Mn_{0.5}O_3$. However, careful examination of the data reveals the possible presence of a peak in this position near to the noise level (less than 1% of the main peak intensity). Attempts to refine a mixture of the *Pnma* and *I*2/*a* structures invariably led to a refined weight fraction of the *Pnma* phase at 1% or less than that of the *I*2/*a* phase. It should be noted that there are reflections of the β-Bi_2O_3 structure present at a nearly identical *d*-spacing, such that the weak peak may relate to an incomplete fitting of an impurity phase present at low levels. Therefore, further analysis of the phases present again leads to the conclusion that the $Bi_{0.3}La_{0.7}Fe_{0.5}Mn_{0.5}O_3$ sample has a monoclinic *I*2/*a* structure.

Due to the observation of a monoclinic cell for $Bi_{0.3}La_{0.7}Fe_{0.5}Mn_{0.5}O_3$, Rietveld refinements were performed on other samples using a monoclinic *I*2/*a* structure. These refinements did not result in an improved fit relative to the *Pnma* structure. Similarly tests were performed to examine the possibility of mixed *Pnma* and *I*2/*a* structures, with no clear evidence for this in the form of an improved fit being found by Rietveld refinement. It was therefore concluded that the space group *Pnma* is preferable in all samples with the exception of $Bi_{0.3}La_{0.7}Fe_{0.5}Mn_{0.5}O_3$, and that other samples are not simply metrically orthorhombic.

A comparison between the expected $GdFeO_3$-type *Pnma* structure and the observed monoclinic *I*2/*a* structure is warranted here. For both space groups, the asymmetric unit contains the same number of crystallographically independent sites: two oxygen sites, one *A* site (Bi,La), and one *B*-site (Fe,Mn). For both structures, the *B*-site is on an inversion center and the *O*2 site is on a general position. However, the *A* and *O*1 sites are on a two-fold axis in the *I*2/*a* structure (4*e* site), while the *A* and *O*1 sites are both on a mirror plane in the *Pnma* structure (4*c* site). As a result, there is one more free parameter to describe the position of these sites in the *Pnma* structure. For example, in the compound $Bi_{0.5}$

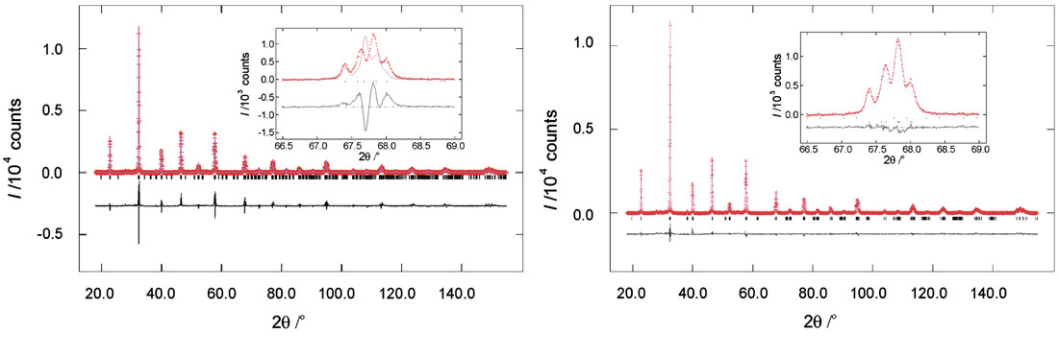

Fig. 4. Comparison of Rietveld refinement results for fit to X-ray diffraction data in the *Pnma* (left) and *I2/a* (right) models in $Bi_{0.3}La_{0.7}Fe_{0.5}Mn_{0.5}O_3$. The fit of the data to the monoclinic model is clearly superior to the orthorhombic model, and provides an improved indexing of the peaks as illustrated for the region near 68° 2θ (insets).

$La_{0.5}Fe_{0.5}Mn_{0.5}O_3$ (*Pnma*) the *A* and *O*1 positions are (0.5115, 0.25, 0.5045) and (0.9970, 0.25, 0.4309), respectively; for $Bi_{0.3}La_{0.7}Fe_{0.5}Mn_{0.5}O_3$ (*I2/a*) the *A* and *O*1 positions are (0.25, 0.9989, 0) and (0.25, 0.4381, 0), respectively. It is clear that the shift in atomic coordinates from *Pnma* to *I2/a* are quite small; the most significant difference appears to be in the movement of the *A* site towards a higher symmetry position in the *I2/a* structure. Just as the differences in coordinates are small, there is a little difference in the bond valence sums (Tables 5, 6 and 7), bond angles, or bond distances (Table 3) for the $Bi_{0.3}La_{0.7}Fe_{0.5}Mn_{0.5}O_3$ ($x=0.3$) phase relative to the $x=0.1$ or 0.5 phases that would suggest a clear crystal chemical reason for the occurrence of the *I2/a* structure.

The *I2/a* monoclinic perovskite structure (the Sr_2CoRuO_6 structure type) is relatively uncommon with only 20 entries in the ICDD database in comparison with the *Pnma* structure ($GdFeO_3$ structure type) that has over 2000 entries. Compounds that have been reported in the Sr_2CoRuO_6 structure type include: Sr_2FeRuO_6, [54] $BaLaZnRuO_6$, $BaLaNiRuO_6$, [54] $La_{0.9}Sr_{0.1}Ga_{0.9}Mg_{0.1}O_{2.9}$, [55] $Ba(Ho_{2/3}Mo_{1/3})O_3$, [56] $(La,Sr)Co_{0.5}Fe_{0.5}O_3$, [57] $Pr_{0.51}Sr_{0.49}FeO_3$, [58] $Pr_{0.6}Sr_{0.4}MnO_3$, [59] $LaCoO_3$, [60] and $LaMnO_3$ [61]. The high pressure phases $BiMnO_3$, $BiScO_3$, and $BiCrO_3$ [62] (the $BiMnO_3$ structure type) have also been reported in this space group, though in this case the unit cell is doubled in volume compared with that of the cell reported here for $Bi_{0.3}La_{0.7}Fe_{0.5}Mn_{0.5}O_3$ [26]; there has been some debate over whether the correct structure is in a centrosymmetric (*C2/c*) or noncentrosymmetric (*Cc* or *C*2) space group for the $BiMnO_3$ phase [63]. The octahedral distortion that produces the *I2/a* (Sr_2CoRuO_6-type) structure corresponds to an $a^-b^-b^-$ type tilting in Glazer notation (tilt system 13) [64–65], involving a small antiphase rotation around one tilt axis (a^-) and a larger antiphase rotation of equal size around two other tilt axes (b^-). Other closely related tilt systems include tetragonal *Imma* ($a^0b^-b^-$), in which one tilt is not present, and $R\bar{3}c$ ($a^-a^-a^-$), in which all of the tilt angles are identical; these are related by symmetry to *I2/a*, as *I2/a* is a subgroup of *Imma* and $R\bar{3}c$. However, *I2/a* is not a subgroup of *Pnma*, and therefore a phase transition between the two structures would have to be first order. In terms of tilting, the difference between the two structures can be described by an anti-phase rotation of the BO_6 octahedra along one direction of the pseudocubic axes in *I2/a* ($a^-b^-b^-$), compared to the in-phase tilting observed in *Pnma* ($a^+b^-b^-$), and is illustrated in Fig. 5 [66].

Octahedral tilting of this type may be caused by the ratio of cation sizes on the *A* and *B*-sites, although other electronic factors may also play a role in the distortion of simple cubic symmetry. The lone-pair of 6*s* electrons for Bi^{3+} is known to play a stereochemically active role, and in the case of the $BiMnO_3$-type structure the lone pairs drive an antiparallel displacement of the bismuth cations that doubles the cell size [63]. In the case of $LaCoO_3$ and $LaMnO_3$, the *I2/a* symmetry occurs in part due to cooperative orbital ordering of Jahn–Teller active d^4 Mn^{3+} cation, or intermediate spin (IS) state in Co^{3+} [60]. In $Pr_{0.6}Sr_{0.4}MnO_3$, the structure is highly dependent on the level of electronic doping and Mn^{3+} content, and the *I2/a* structure may occur in coexistence with the *Pnma* structure due to slight inhomogeneities in composition [59]. It is likely that a subtle difference in the electronic structure related to hole doping (bismuth deficiency and oxygen excess), possibly in combination with the stereochemical influence of the Bi^{3+} lone-pair, is the cause of the *I2/a* structure in $Bi_{0.3}La_{0.7}Fe_{0.5}Mn_{0.5}O_3$. A systematic study of the relationship between composition and structure would likely lead to the observation of the *I2/a* structure in other members of the $Bi_xLa_{1-x}Fe_{0.5}Mn_{0.5}O_3$ series. Further investigation into the relationship between doping level, structure, and properties for $Bi_xLa_{1-x}Fe_{0.5}Mn_{0.5}O_3$ is warranted to examine the potential impact on multiferroic behavior [30].

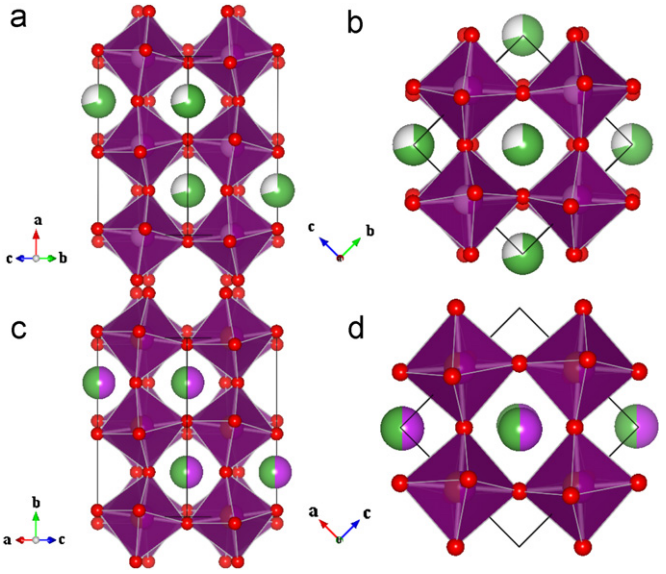

Fig. 5. Comparison of octahedral tilting for $Bi_{0.3}La_{0.7}Fe_{0.5}Mn_{0.5}O_3$ in the *I2/a* structure (a,b), and $Bi_{0.5}La_{0.5}Fe_{0.5}Mn_{0.5}O_3$ in the *Pnma* structure (c,d). Antiphase octahedral tilting occurs along the long axis in (b) for the *I2/a* structure, while in-phase tilting occurs in (d) for the *Pnma* structure.

3.5. Thermal expansion

Thermal expansion occurs in a positive fashion for all axes in the case of $Bi_xLa_{1-x}Fe_{0.5}Mn_{0.5}O_3$, as seen in Fig. 6. However, in the case of $Bi_xNd_{1-x}Fe_{0.5}Mn_{0.5}O_3$ negative thermal expansion along the *a* axis occurs above the temperature range ~100–150 K for $x=0.3$, and approximately zero thermal expansion above 150 K for $x=0.5$ (Fig. 7). A similar temperature-dependence is observed in the end-member $NdFe_{0.5}Mn_{0.5}O_3$, for which this lattice

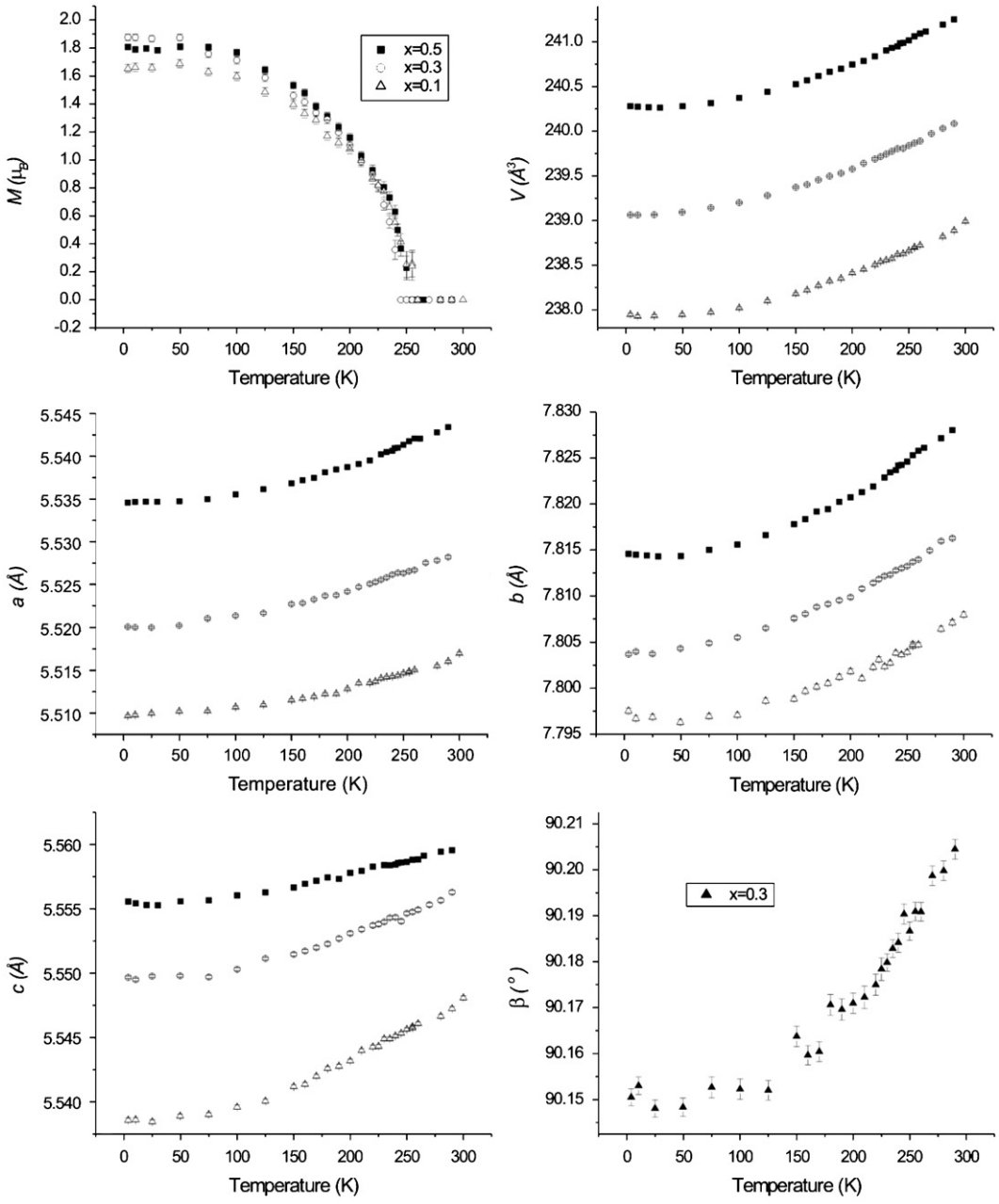

Fig. 6. Variation in magnetic moment per mole of formula unit, and lattice parameters versus temperature, for $Bi_xLa_{1-x}Fe_{0.5}Mn_{0.5}O_3$.

parameter is reported to decrease from 5.6281 Å at 4.3 K to 5.6241 Å at 290 K [43]. A comparison may be made with the orthoferrite $NdFeO_3$, which undergoes long-range antiferromagnetic order below $T_N = 760$ K and also crystallizes in the $GdFeO_3$-type structure; this member of the $REFeO_3$ series exhibits a maximum in the *a* lattice parameter near 40 K, and a minimum near 160 K [67]. In $NdFeO_3$, the variation in the *a* lattice parameter is correlated with a reorientation in the ordered magnetic moment, which occurs between 100 and 200 K; for the *Pnma* space group setting, the moments are oriented along the *z* direction above 200 K, with a *y* component mixing in below 200 K. This produces an increase in the $(1\,3\,0)_m$ reflection intensity and a decrease in the $(1\,1\,2)_m$ reflection intensity below 200 K. This magnetic peak intensity variation is not observed in samples of $Bi_xNd_{1-x}Fe_{0.5}Mn_{0.5}O_3$, suggesting that the spin reorientation is quenched; the moment is oriented along the *y* direction at all temperatures. Interestingly, strong magnetoelastic effects are also observed in $NdMnO_3$ resulting in abrupt changes in the lattice parameters below the antiferromagnetic ordering temperature $T_N \approx 82$ K [68]. In the case of $Bi_xNd_{1-x}Fe_{0.5}Mn_{0.5}O_3$, the negative thermal expansion continues beyond the magnetic ordering temperature, with no significant feature indicative of coupling with the magnetic order. It appears that the random occupation of Mn and Fe on the *B*-site leads to quenching of these strong magnetoelastic effects. Therefore, the negative thermal expansion is more likely to be structural, and associated with the approach to a higher temperature structural phase transition.

To further investigate how the lattice parameters for the neodymium phases vary with temperature, it is useful to parameterize the deviation from a tetragonal lattice as the orthorhombic strain (e_{ortho}). The orthorhombic strain is defined here as

$$e_{ortho} = (a-c)/(a+c) \quad (2)$$

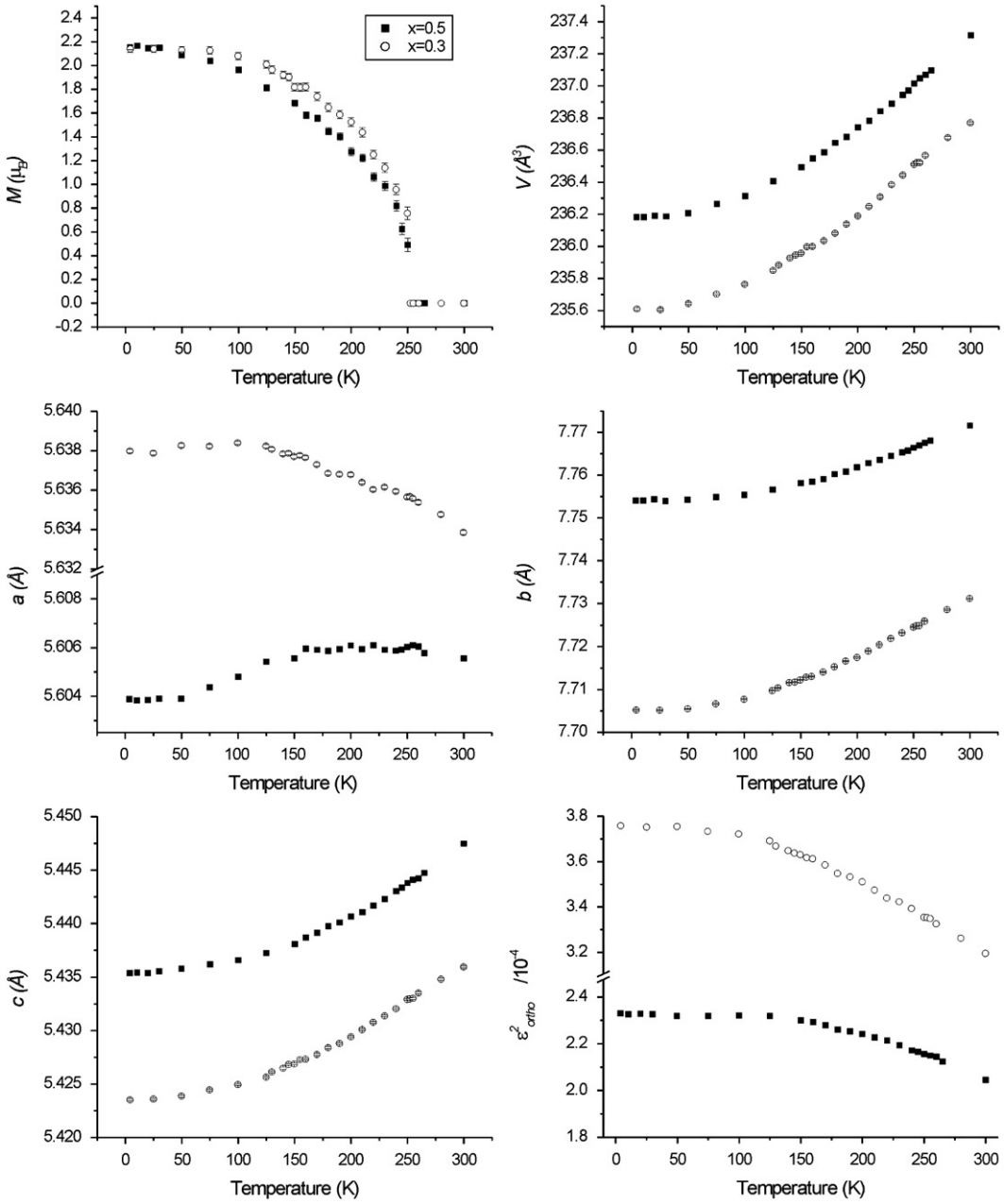

Fig. 7. Variation in magnetic moment per mole of formula unit, and lattice parameters versus temperature, for $Bi_xNd_{1-x}Fe_{0.5}Mn_{0.5}O_3$. The figure in the bottom right displays a plot of orthorhombic strain, indicating that the difference between the *a* and *c* lattice parameters of the *Pnma* perovskite structure is decreasing with an increasing temperature.

where *a* and *c* are for the shorter lattice parameters in the $GdFeO_3$-type structure (parameters at $\sim\sqrt{2}a_p$) [69]. The square of the orthorhombic strain has been plotted in Fig. 7 to further investigate the thermal expansion, with the expectation that a transition to a higher symmetry will take place at the point where $c=a$, assuming the transition would be continuous. An extrapolation of the linear portion of the orthorhombic strain vs. temperature plot between 200 and 300 K suggests that an equivalence between *c* and *a* could occur near 1100 °C for $x=0.3$ and 180 °C for $x=0.5$ of the $Bi_xNd_{1-x}Fe_{0.5}Mn_{0.5}O_3$ series. This can only be taken as a rough estimate given that the observed data is over a significantly lower temperature range, and that lattice parameters for this trend are estimated from 2.37 Å wavelength neutron diffraction data that provide relatively few reflections. Preliminary investigations via in-situ XRD up to 925 °C did not reveal any evidence of a structural phase transition, and were complicated by the relatively poor stability of compounds in the temperature range of interest; further investigations for a higher temperature are planned.

3.6. Magnetic susceptibility

DC magnetic susceptibility data are shown in Fig. 8. These data do not extend to a sufficiently high temperature above the magnetic transition to examine the paramagnetic (PM) moment, using Curie–Weiss law. A magnetic transition in the temperature range 240–245 K for $Bi_xLa_{1-x}Fe_{0.5}Mn_{0.5}O_3$ samples and 240–255 K for $Bi_xNd_{1-x}Fe_{0.5}Mn_{0.5}O_3$ are suggested by the position of the minimum in a plot of $\delta(\chi T)/\delta T$ (known as Fisher heat capacity) [70]. Antiferromagnetic (AFM) ordering temperatures (T_N) that have been estimated from the minimum in Fisher heat capacity are summarized in Table 2. For all samples, the

temperature-dependence of the susceptibility data below the transition is suggestive of a weak ferromagnetic (FM) component, as is clearly demonstrated by the rapid rise in χT below the transition temperature. A further indication of cooperative magnetic order is given by the divergence between the zero-field-cooled (ZFC) and field-cooled (FC) data for all the samples. The ferromagnetic component may arise from superparamagnetic-like clusters within the sample, which may freeze at low temperature resulting in a drop in the ZFC susceptibility.

3.7. Variable temperature refinement of magnetic neutron diffraction data

Magnetic reflections were indexed readily at ~4 K to the nuclear unit cell (Fig. 9), indicating a propagation vector (**k**) for the magnetic unit cell of (0,0,0). The relative intensities of the magnetic peaks are consistent with a G_y-type antiferromagnetic structure (Fig. 10), indicating dominant AFM coupling along all M–O–M nearest neighbor magnetic exchange pathways (Fig. 8). This is in agreement with reports of a G-type structure for the $LaFe_{0.5}Mn_{0.5}O_3$ and $NdFe_{0.5}Mn_{0.5}O_3$ end-members [43,44].

The temperature-dependence of the magnetic ordering was examined for each sample by fitting the temperature variation of the magnetic moment to a power law given by [71]

$$\mu = A[(T-T_N)/T_N]^{\beta} \quad (3)$$

Here β is the critical exponent, A is a constant, and μ is the magnetic moment. The critical exponents are in the range 0.26(2)–0.34(1); these values in some cases are not consistent with the result expected for 3D antiferromagnets (Ising 0.326, *XY* 0.345, and Heisenberg 0.367). This may indicate that the power law is not well adhered to over a wide temperature range in these samples, and that more data are required near the ordering transition to obtain more accurate values. These results are summarized in Table 2, and provide another estimate of the magnetic ordering temperatures. The ordering temperatures derived from the magnetic susceptibility data (Fisher heat capacity) agree very well with the results of the power law fit in the case of the $Bi_xLa_{1-x}Fe_{0.5}Mn_{0.5}O_3$ series and the $Bi_{0.3}Nd_{0.7}Fe_{0.5}Mn_{0.5}O_3$ sample. In the case of the $Bi_{0.1}Nd_{0.9}Fe_{0.5}Mn_{0.5}O_3$ sample, temperature-dependent PND data are not available; the Fisher heat capacity plot in the region of the ordering transition shows an overall temperature-dependence that is similar to the $Bi_{0.5}Nd_{0.5}Fe_{0.5}Mn_{0.5}O_3$ sample, and the minimum is near 240 K for $x=0.1$ as compared to 242 K for $x=0.5$.

There is a discrepancy in the case of $Bi_{0.5}Nd_{0.5}Fe_{0.5}Mn_{0.5}O_3$, such that the ordering temperature derived from a power law fit to the neutron data ($T_N=252(1)$ K) is significantly higher than that from Fisher heat capacity (T_N~242 K). Estimation of the ordering temperature from the susceptibility data may be hindered

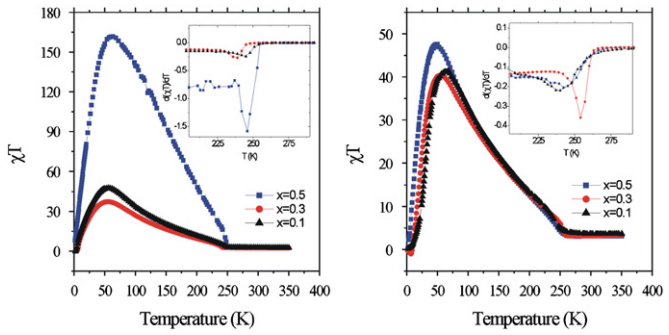

Fig. 8. DC magnetic susceptibility data of $Bi_xRE_{1-x}Fe_{0.5}Mn_{0.5}O_3$, with *RE*=La (left) and *RE*=Nd (right). Data were collected at 0.1 T for all samples, with the exception of $Bi_{0.5}La_{0.5}Fe_{0.5}Mn_{0.5}O_3$ for which the applied field was 1 T. The χT plots are derived from ZFC data.

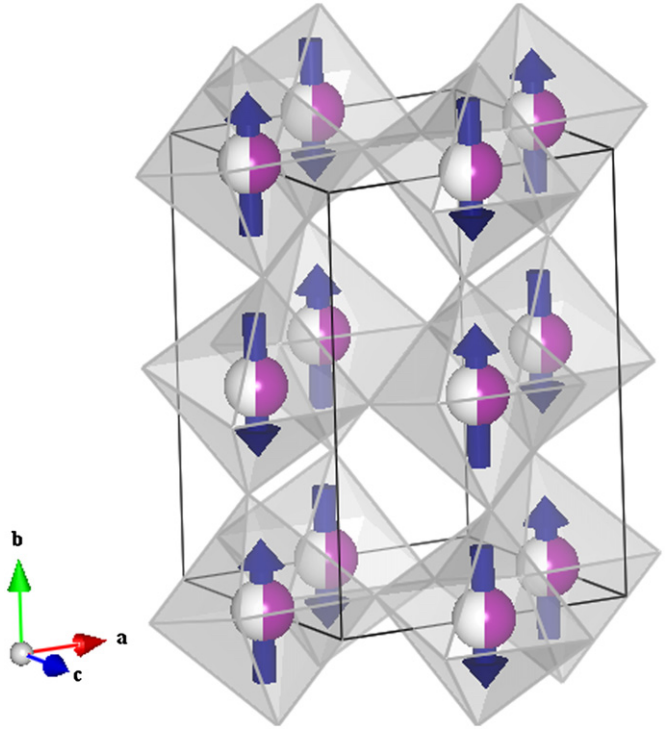

Fig. 10. G-type antiferromagnetic magnetic structure with a propagation vector **k**=(0 0 0). Spheres correspond to *B*-site cations at the center of BO_6 octahedra. *A*-site cations are removed for clarity.

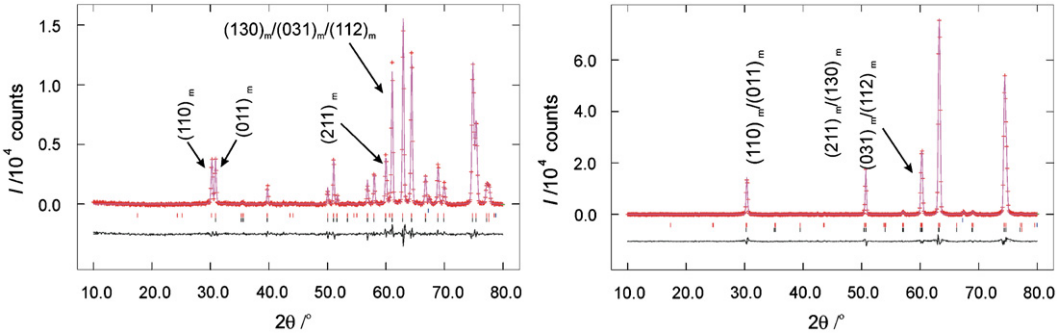

Fig. 9. Rietveld refinement of powder neutron diffraction data collected at 4 K for $Bi_{0.5}Nd_{0.5}Fe_{0.5}Mn_{0.5}O_3$ (left) and $Bi_{0.5}La_{0.5}Fe_{0.5}Mn_{0.5}O_3$ (right). The peaks with magnetic contributions are indexed using the **k**=(0 0 0) propagation vector, indicating that the magnetic unit cell is identical to that of the non-magnetic unit cell.

by the influence of experimental parameters that affect the shape of curve, such as applied magnetic field and ramp rate. A visual examination of the magnetic peak intensity for this sample clearly indicates the presence of peaks at 245 K, and despite significant noise that these peaks have a very small intensity remaining at 250 K. Therefore, the result of a power law fit to the neutron diffraction data will be considered a more reliable estimate of T_N for this sample. A visual inspection of the PND data for the $Bi_xLa_{1-x}Fe_{0.5}Mn_{0.5}O_3$ series demonstrates that the magnetic peak intensity disappears above 240 K and below 250 K, suggesting that the ordering temperatures for the neodymium samples may be systematically higher than in the lanthanum case. This is in agreement with the trend for the end-members $LaFe_{0.5}Mn_{0.5}O_3$ and $NdFe_{0.5}Mn_{0.5}O_3$, with antiferromagnetic ordering temperatures of 260 and 300 K, respectively, [43,44] indicating stronger antiferromagnetic superexchange interactions for $NdFe_{0.5}Mn_{0.5}O_3$. Relative to the end-members, the substitution of Bi^{3+} for RE^{3+} led to an immediate drop in the ordering temperature of ~20 K for the La^{3+}-containing series and ~50 K for the Nd^{3+} containing series. It appears that by $x=0.1$, the disordered lattice strain imposed by the lone-pair on bismuth is capable of disrupting long-range-ordered antiferromagnetic interactions.

The magnetic moments of the $Bi_xNd_{1-x}Fe_{0.5}Mn_{0.5}O_3$ series (2.14–2.15 μ_B/mol f.u.) are systematically higher than those of the $Bi_xLa_{1-x}Fe_{0.5}Mn_{0.5}O_3$ series (1.66–1.88 μ_B/mol f.u.). Though an intermediate spin state of $t_{2g}^4e_g^1$ has been suggested for the d^5 Fe^{3+} cation in $LaFe_{0.5}Mn_{0.5}O_3$ [72], the high spin state is generally expected due to the relatively weak metal-oxide crystal field interaction [73]. This corresponds to $t_{2g}^3e_g^2$ ($S=5/2$) for Fe^{3+}, $t_{2g}^3e_g^1$ ($S=2$) for Mn^{3+} and $t_{2g}^3e_g^0$ ($S=3/2$) Mn^{4+} cations. As magnetic neutron diffraction intensities are given by $2S$, the observed moments are expected to be in the range of 4.5 μ_B for a mixture of Mn^{3+}/Fe^{3+}, or slightly lower as oxidation occurs to form Mn^{4+}. The moment refined from the powder neutron diffraction data for ordering on the transition metal sublattice is significantly lower than that may be expected from complete ordering of Mn^{3+} and Fe^{3+} cations. Similar results were observed in the case of $NdFe_{0.5}Mn_{0.5}O_3$, with an ordered moment of 2.2 μ_B at 4.3 K, indicating that the low ordered moment is not simply related to the introduction of bismuth in the lattice [43]. The reduced moment occurs mainly as a result of disorder on the *B*-site. Due to similar cation size and charge of Mn^{3+} (0.645 Å) and Fe^{3+} (0.645 Å) cations [74–75], there is no driving force for them to order on the perovskite lattice. The resulting disorder produces a range of competing superexchange interactions including: AFM Fe^{3+}–O–Fe^{3+} spin interactions for t^3–O–t^3 and e^2–O–e^2 exchange; AFM Mn^{3+}–O–Mn^{3+} t^3–O–t^3 interactions; FM Mn^{3+}–O–Mn^{4+} e^1–O–e^0 interactions. The Fe^{3+}–O–Mn^{3+} spin interactions are predominantly ferromagnetic, and in addition to FM Mn^{3+}–O–Mn^{4+} superexchange interactions may be responsible for the FM component in the magnetic susceptibility data [30]. The competition between AFM and FM interactions leads to a cluster-glass like behavior, reflected by a divergence between the ZFC and FC data in the susceptibility data (Fig. 8). Domains of AFM and FM exchange are present, with larger AFM domains occurring in the $Bi_xNd_{1-x}Fe_{0.5}Mn_{0.5}O_3$ series of samples due to stronger AFM interactions, leading to a larger magnetic moment and higher ordering temperature than in the $BiLa_{1-x}Fe_{0.5}Mn_{0.5}O_3$ series. There is no evidence from these data for an ordered Nd^{3+} magnetic moment above 4 K, which could arise from polarization of the neodymium moments in the presence of ordering on the *B*-site. The magnetic susceptibility and magnetic neutron diffraction results taken together are consistent with the presence of both spin-glass and long-range-ordered components, leading to a reduced moment for the G-type antiferromagnetic structure for all samples.

4. Conclusions

The bismuth substituted phases $Bi_xRE_{1-x}Fe_{0.5}Mn_{0.5}O_{3+\delta}$ (RE= La,Nd) have been prepared at an ambient pressure for $x \leq 0.5$. The samples undergo a transition to G-type antiferromagnetic order along with a weak ferromagnetic component, mixed with cluster-glass type behavior. Long range ordering temperatures T_N in the range 240–255 K were observed with a significantly lower ordered magnetic moment in the case of lanthanum (M~1.7–1.9 μ_B) than in the case of neodymium (M~2.1 μ_B). The substitution of bismuth into the lattice results in a drop in T_N relative to the lanthanide end-members, but exhibits no clear correlation with the magnitude of the ordered moment on the *B*-site. Bond valence and Rietveld refinement results suggest that the oxidation states are a mixture of Fe^{3+} and Mn^{3+}, along with some oxidation to form Mn^{4+} corresponding to an oxygen excess δ~0.01–0.07. There is no evidence for a low temperature structural phase transition in any sample, indicating that the average structures remain centrosymmetric. Large ADP parameters in the $Bi_xLa_{1-x}Fe_{0.5}Mn_{0.5}O_{3+\delta}$ samples may reflect a local structural distortion related to the Bi^{3+} lone-pair that could promote the weak ferroelectric-like behavior reported in $Bi_{0.5}La_{0.5}Fe_{0.5}Mn_{0.5}O_3$. Crystal structures in both series were determined to be $GdFeO_3$-type *Pnma* with the exception of the $Bi_{0.3}La_{0.7}Fe_{0.5}Mn_{0.5}O_{3+\delta}$ sample, which is monoclinic *I2/a* in the $a^-b^-b^-$ tilt scheme.

Acknowledgments

We acknowledge Ashfia Huq and Jason Hodges for collection of powder neutron diffraction data on the $Bi_{0.1}Nd_{0.9}Fe_{0.5}Mn_{0.5}O_3$ sample at the Spallation Neutron Source. We thank Larry Walker of the High Temperature Materials Laboratory at Oak Ridge National Laboratory for collection of the microprobe data, which was collected at ORNL's SHaRE User Facility. We thank Ian Swainson of Chalk River Laboratories for a critical reading of the manuscript. Research at the SHaRE User Facility and the SNS was sponsored by the Scientific User Facilities Division, Office of Basic Energy Sciences, U.S. Department of Energy. Research at ORNL was sponsored by the Materials Sciences and Engineering Division, Office of Basic Energy Sciences, U. S. Department of Energy.

Appendix A. Supporting material

Supplementary data associated with this article can be found in the online version at doi:10.1016/j.jssc.2011.02.006.

References

[1] M. Fiebig, T. Lottermoser, D. Frohlich, A.V. Goltsev, R.V. Pisarev, Nature 419 (2002) 818.
[2] T. Kimura, T. Goto, H. Shintani, K. Ishizaka, T. Arima, Y. Tokura, Nature 426 (2003) 55.
[3] T. Goto, T. Kimura, G. Lawes, A.P. Ramirez, Y. Tokura, Physical Review Letters 92 (2004) 257201.
[4] K. Taniguchi, N. Abe, T. Takenobu, Y. Iwasa, T. Arima, Physical Review Letters 97 (2006) 097203.
[5] D. Meier, M. Maringer, T. Lottermoser, P. Becker, L. Bohaty, M. Fiebig, Physical Review Letters 102 (2009) 107202.
[6] S. Ishiwata, Y. Taguchi, H. Murakawa, Y. Onose, Y. Tokura, Science 319 (2008) 1643.
[7] J. van Suchtelen, Philips Research Reports 27 (1972) 28.
[8] G. Srinivasan, E.T. Rasmussen, J. Gallegos, R. Srinivasan, Y.I. Bokhan, V.M. Laletin, Physical Review B 6421 (2001) 214408.
[9] G. Srinivasan, E.T. Rasmussen, B.J. Levin, R. Hayes, Physical Review B 65 (2002) 134402.

[10] J. Wang, J.B. Neaton, H. Zheng, V. Nagarajan, S.B. Ogale, B. Liu, D. Viehland, V. Vaithyanathan, D.G. Schlom, U.V. Waghmare, N.A. Spaldin, K.M. Rabe, M. Wuttig, R. Ramesh, Science 299 (2003) 1719.
[11] M. Valant, A.K. Axelsson, N. Alford, Chemistry of Materials 19 (2007) 5431.
[12] G. Catalan, J.F. Scott, Advanced Materials 21 (2009) 2463.
[13] S.M. Selbach, M.A. Einarsrud, T. Grande, Chemistry of Materials 21 (2009) 169.
[14] S.M. Selbach, T. Tybell, M.A. Einarsrud, T. Grande, Advanced Materials 20 (2008) 3692.
[15] R. Ramesh, Nature 461 (2009) 1218.
[16] H. Hughes, M.M.B. Allix, C.A. Bridges, J.B. Claridge, X.J. Kuang, H.J. Niu, S. Taylor, W.H. Song, M.J. Rosseinsky, Journal of the American Chemical Society 127 (2005) 13790.
[17] T. Atou, H. Chiba, K. Ohoyama, Y. Yamaguchi, Y. Syono, Journal of Solid State Chemistry 145 (1999) 639.
[18] P. Baettig, R. Seshadri, N.A. Spaldin, Journal of the American Chemical Society 129 (2007) 9854.
[19] C.A. Bridges, M. Allix, M.R. Suchomel, X.J. Kuang, I. Sterianou, D.C. Sinclair, M.J. Rosseinsky, Angewandte Chemie-International Edition 46 (2007) 8785.
[20] M.R. Suchomel, C.I. Thomas, M. Allix, M.J. Rosseinsky, A.M. Fogg, M.F. Thomas, Applied Physics Letters 90 (2007) 112909.
[21] C.H. Yang, J. Seidel, S.Y. Kim, P.B. Rossen, P. Yu, M. Gajek, Y.H. Chu, L.W. Martin, M.B. Holcomb, Q. He, P. Maksymovych, N. Balke, S.V. Kalinin, A.P. Baddorf, S.R. Basu, M.L. Scullin, R. Ramesh, Nature Materials 8 (2009) 485.
[22] H. Uchida, R. Ueno, H. Funakubo, S. Koda, Journal of Applied Physics 100 (2006) 014106.
[23] V.A. Khomchenko, D.A. Kiselev, J.M. Vieira, A.L. Kholkin, M.A. Sa, Y.G. Pogorelov, Applied Physics Letters 90 (2007) 242901.
[24] S.M. Selbach, T. Tybell, M.A. Einarsrud, T. Grande, Chemistry of Materials 21 (2009) 5176.
[25] I. Sosnowska, W. Schaffer, W. Kockelmann, K.H. Andersen, I.O. Troyanchuk, Applied Physics a-Materials Science & Processing 74 (2002) S1040.
[26] M. Azuma, H. Kanda, A.A. Belik, Y. Shimakawa, M. Takano, Journal of Magnetism and Magnetic Materials 310 (2007) 1177.
[27] G. Kartopu, A. Lahmar, M. Es-Souni, Applied Physics Letters 92 (2008) 151910.
[28] A. Lahmar, S. Habouti, C.H. Solterbeck, M. Es-Souni, B. Elouadi, Journal of Applied Physics 105 (2009) 014111.
[29] V.V. Gagulin, S.K. Korchagina, Y.A. Shevchuk, N.V. Fadeeva, V.V. Bogatko, Ferroelectrics 204 (1997) 345.
[30] A.K. Kundu, R. Ranjith, B. Kundys, N. Nguyen, V. Caignaert, V. Pralong, W. Prellier, B. Raveau, Applied Physics Letters 93 (2008) 052906.
[31] Y. Tokunaga, N. Furukawa, H. Sakai, Y. Taguchi, T. Arima, Y. Tokura, Nature Materials 8 (2009) 558.
[32] K. Ramesha, A. Llobet, T. Proffen, C.R. Serrao, C.N.R. Rao, Journal of Physics-Condensed Matter 19 (2007) 102202.
[33] H.M. Rietveld, Journal of Applied Crystallography 2 (1969) 65.
[34] A.C., Larson, R.B., von Dreele, LANSCE (1994).
[35] B.H. Toby, Journal of Applied Crystallography 34 (2001) 210.
[36] J. Rodriguez-Carvajal, Physica 192B (1993) 55.
[37] T., Roisnel, J., Rodriguez-Carvajal, Epdic 7: European Powder Diffraction, Pts 1 and 2 378-3 (2001) 118.
[38] A.M. Glazer, Acta Crystallographica Section B-Structural Science B 28 (1972) 3384.
[39] C.J. Howard, H.T. Stokes, Acta Crystallographica Section B-Structural Science 54 (1998) 782.
[40] C.J. Howard, H.T. Stokes, Acta Crystallographica Section B-Structural Science 58 (2002) 565.
[41] C.J. Howard, H.T. Stokes, Acta Crystallographica Section B-Structural Science 60 (2004) 674.
[42] C.J. Howard, H.T. Stokes, Acta Crystallographica Section A 61 (2005) 93.
[43] I.O. Troyanchuk, M.V. Bushinsky, H. Szymczak, M. Baran, K. Barner, Journal of Magnetism and Magnetic Materials 312 (2007) 470.
[44] X.D. Zhou, L.R. Pederson, Q. Cai, J. Yang, B.J. Scarfino, M. Kim, W.B. Yelon, W.J. James, H.U. Anderson, C. Wang, Journal of Applied Physics 99 (2006) 08M918.
[45] X.D. Zhou, J.B. Yang, E.C. Thomsen, Q. Cai, B.J. Scarfino, Z. Nie, G.W. Coffey, W.J. James, W.B. Yelon, H.U. Anderson, L.R. Pederson, Journal of the Electrochemical Society 153 (2006) J133.
[46] W. Pitschke, H. Hermann, N. Mattern, Powder Diffraction 8 (1993) 74.
[47] R. Seshadri, N.A. Hill, Chemistry of Materials 13 (2001) 2892.
[48] J. Topfer, J.B. Goodenough, Chemistry of Materials 9 (1997) 1467.
[49] I.D. Brown, Chemical Reviews 109 (2009) 6858.
[50] V. Sidey, Acta Crystallographica Section B-Structural Science 62 (2006) 949.
[51] V. Sidey, Acta Crystallographica Section B-Structural Science 64 (2008) 515.
[52] A.L., Speck, Utrecht University, Utrecht (2001).
[53] Y. Lepage, Journal of Applied Crystallography 21 (1988) 983.
[54] P.D. Battle, T.C. Gibb, C.W. Jones, F. Studer, Journal of Solid State Chemistry 78 (1989) 281.
[55] M. Kajitani, M. Matsuda, A. Hoshikawa, S. Harjo, T. Kamiyama, T. Ishigaki, F. Izumi, M. Miyake, Journal of Physics and Chemistry of Solids 68 (2007) 758.
[56] S. Oyama, Y. Doi, Y. Hinatsu, Y. Ishii, Bulletin of the Chemical Society of Japan 77 (2004) 1359.
[57] K. Swierczek, B. Dabrowski, L. Suescun, S. Kolesnik, Journal of Solid State Chemistry 182 (2009) 280.
[58] V.V. Kharton, M.V. Patrakeev, J.C. Waerenborgh, A.V. Kovalevsky, Y.V. Pivak, P. Gaczynski, A.A. Markov, A.A. Yaremchenko, Journal of Physics and Chemistry of Solids 68 (2006) 355.
[59] C. Ritter, P.G. Radaelli, M.R. Lees, J. Barratt, G. Balakrishnan, D.M. Paul, Journal of Solid State Chemistry 127 (1996) 276.
[60] J.B., Goodenough, Reports on Progress in Physics 67 (2004) 1915.
[61] A. Maignan, C. Michel, M. Hervieu, B. Raveau, Solid State Communications 101 (1997) 277.
[62] A.A. Belik, S. Iikubo, K. Kodama, N. Igawa, S. Shamoto, E. Takayama-Muromachi, Chemistry of Materials 20 (2008) 3765.
[63] A.A. Belik, S. Iikubo, K. Kodama, N. Igawa, S. Shamoto, M. Maie, T. Nagai, Y. Matsui, S.Y. Stefanovich, B.I. Lazoryak, E. Takayama-Muromachi, Journal of the American Chemical Society 128 (2006) 706.
[64] P.M. Woodward, Acta Crystallographica Section B-Structural Science 53 (1997) 44.
[65] P.M. Woodward, Acta Crystallographica Section B-Structural Science 53 (1997) 32.
[66] K. Momma, F. Izumi, Journal of Applied Crystallography 41 (2008) 653.
[67] W. Slawinski, R. Przenioslo, I. Sosnowska, M. Brunelli, M. Bieringer, Nuclear Instruments & Methods in Physics Research Section B-Beam Interactions with Materials and Atoms 254 (2007) 149.
[68] T. Chatterji, B. Ouladdiaf, D. Bhattacharya, Journal of Physics-Condensed Matter 21 (2009) 306001.
[69] B.J. Kennedy, C.J. Howard, Y. Kubota, K. Kato, Journal of Solid State Chemistry 177 (2004) 4552.
[70] M.E. Fisher, Philosophical Magazine 7 (1962) 1731.
[71] M.F. Collins, Magnetic Critical Scattering, Oxford University Press, Oxford, 1989.
[72] W. Tong, B. Zhang, S. Tan, Y.H. Zhang, Physical Review B 70 (2004) 014422.
[73] S.D. Bhame, V.L.J. Joly, P.A. Joy, Physical Review B 72 (2005) 054426.
[74] R.D. Shannon, C.T. Prewitt, Acta Crystallographica Section B-Structural Crystallography and Crystal Chemistry 25 (1969) 925B 25 (1969) 925.
[75] R.D. Shannon, C.T. Prewitt, Acta Crystallographica Section B-Structural Crystallography and Crystal Chemistry 26 (1970) 1046.